LAWRENCE
LIVERMORE
NATIONAL
LABORATORY

LLNL-JRNL-774079

Orientation Relationships of Pure Tin on Single Crystal Germanium Substrates

T. C. Reeve, S. T. Reeve, C. A. Handwerker

May 13, 2019

Journal of Electronic Materials

Disclaimer

ORIENTATION RELATIONSHIPS OF PURE TIN ON SINGLE CRYSTAL GERMANIUM SUBSTRATES

THOMAS C. REEVE [2, 4], SAMUEL TEMPLE REEVE [2, 5] AND CAROL A. HANDWERKER [1, 3] *

1. – Purdue University, School of Materials Engineering, 701 West Stadium Ave., West Lafayette, IN, 47907, USA. 2. – Materials Science Division, Lawrence Livermore National Laboratory, Livermore, CA, 94550, USA. 3. – tel.: +1-765-494-0147, fax: +1-765-494-1204, email: handwerker@purdue.edu. 4. –email: reeve6@llnl.gov. 5. –email: reeve5@llnl.gov

LLNL-JRNL-774079

* Corresponding author: C. A. Handwerker

ABSTRACT

The limited number of independent β-Sn grain orientations resulting from the difficulty in nucleating β-Sn during solidification of Sn-based solders has a large effect on the resulting β-Sn grain size and, hence, on overall solder joint performance and reliability. This study analyzes the efficacy of Ge as a heterogeneous nucleation agent for β-Sn by observing the morphologies and orientation relationships of as-deposited, solid-state annealed, and liquid-state annealed pure Sn films on single crystal Ge (100), (110), and (111) substrates. Results from scanning electron microscopy (SEM) and electron backscatter diffraction (EBSD) showed that the as-deposited Sn films all deposited with a Sn (001) || z-axis texture, regardless of the underlying Ge substrate orientation. Solid-state annealing at 150 °C for 5 min did not result in significant dewetting of the Sn films, and the films maintained their as-deposited texture of Sn (001) || z-axis, regardless of the underlying Ge substrate orientation. Liquid-state annealing at 235 °C for 1 min resulted is large-scale dewetting of the Sn films and re-orientation of the Sn films on the various Ge substrates. After solidification, the Ge (100) and (110) single crystal substrates produced patches of dewetted grains of the same orientation but there were no consistent Sn grain textures after liquid-state annealing, suggesting no single orientation relationship. In contrast, solidification on Ge (111) single crystal substrates resulted in isolated grains with a single Sn film texture and an orientation relationship of $(100)_{Sn} \parallel (111)_{Ge}$ and $[100]_{Sn} \parallel [110]_{Ge}$. Density Functional Theory simulations of the experimentally observed Ge (111) sample orientation relationship and the Ge/Sn cube-on-cube orientation relationship suggest favorable relative interfacial binding energies for both interface orientations.

KEY WORDS: Pb-free solder; β-Sn nucleation; β-Sn inoculation; electron backscatter diffraction

INTRODUCTION

Understanding and control of β-Sn crystal nucleation mechanisms and growth in lead-free, Sn-based solder alloys are ongoing research goals within the microelectronics community. While this is an issue with conventionally sized solder joints, the ability to increase the nucleation of β-Sn in solder joints to form a smaller grain size is of increasing importance as the size of microelectronic solder joints continues to decrease. From the point of view of solder joint properties, the body-centered tetragonal (BCT) crystal structure of β-Sn is highly anisotropic, influencing the physical properties of the crystal, including, elasticity, thermal expansion, resistivity, and diffusivity, particularly under dynamic thermal and mechanical stress gradients. Thus, having only few crystallographic orientations of β-Sn grains in a single solder joint contributes strongly to the thermomechanical response of the joint itself. [1] Having few grains present in each joint combined with the orientation of the grains being uncontrolled leads to both variability in solder joint response and decreased ability for the joints to respond to applied strains by creep. This limited number of grains is related to the significant undercooling long observed in β-Sn alloys, typically between 15 °C to 40 °C in solder joints, with little predictability. [2], [3] This pronounced undercooling is a result of difficulty in homogeneous and heterogeneous nucleation from the melt. [4]–[8], [9]–[11] The difficulty in nucleating β-Sn during solidification produces a number of well-known microstructural characteristics of solder joints: a small number of unique β-Sn dendrites, reproducible twinning structures, and relatively large β-Sn grain sizes. [2], [12], [13] When the difficulty in β-Sn homogeneous nucleation (and even heterogeneous nucleation) and the resulting large, twinned grain structures are considered together, significant variability, both in terms of mechanical and thermal properties, often occurs from joint to joint in a single microelectronic device. [1], [14] Control over the β-Sn nucleation process resulting in smaller grain sizes may reduce microstructural variability joint-to-joint, increase predictability of the overall response of solder joints under various operating conditions, and possibly improve solder joint reliability.

As is well known in the solidification literature increasing the nucleation rate during solidification and promotion of grain refinement in metallic alloys are achieved through the addition of two main components to the alloy liquid:

(1) a potent inoculant phase to enhance the nucleation of the solid phase, and

(2) an excess solute, often know as a growth-restricting solute, to promote a phenomena called constitutional undercooling, a process by which the solute acts to slow the progression of the solid/liquid interface, providing additional undercooling and allowing time for the activation of multiple nucleation sites in the melt and thus promoting grain refinement.

The classic example of grain size refinement combining these approaches is in Al-based alloys, where grain refinement is achieved with the additions of TiB_2 particles as the inoculant phase and Ti solute to promote constitutional undercooling. [15] Research into applying such processes to the β-Sn phase in solder alloys has been an area of active interest. As reviewed previously by Reeve et al. in [16], and more recently by Shang et al. [17], options for effective growth-restricting solutes are limited for Sn, attributed to the low solubility of most elements in Sn. By calculating the "growth-restriction factor", *Q*, one can survey viable solute options for promotion of constitutional undercooling by considering various thermodynamic parameters, including: the liquidus slope, *m*, the partition coefficient, *k*, the alloy solute concentration, c_o, for a binary alloy as seen in Equation 1 below:

$$Q = m(k-1)c_o \quad (1)$$

Solute additions with notable solubility in Sn, including, Zn, Cd, Pb, and Bi, have maximum *Q*-values ranging from ~30-55 K, at their respective solubility limits. [17] In comparison, the *Q*-value for Ti solute in Al is ~37 K at the peritectic composition of 0.15 wt. %, a far lower concentration than necessary to achieve similar *Q*-values with solute additions to Sn alloys. [18]

In addition to solute additions, a potent inoculation phase is required to increase nucleation sites in the liquid alloy. Seminal research analyzing the efficacy of β-Sn nucleation catalysts has revealed several transition metal stannide intermetallic compounds (IMCs) with favorable orientation relationships with β-Sn. Particularly effective were the phases of $\alpha CoSn_3$, $PtSn_4$, and $\beta IrSn_4$. [19]–[21] In particular, Ma et al. used lattice matched β-Sn catalysts, $\alpha CoSn_3$, $PtSn_4$, and $\beta IrSn_4$, to create single crystal solder joints where the orientation of the single β-Sn grain was set by the orientation of the underlaying nucleating crystal seed attached directly to the solder joint substrate. [19] Not only did this work highlight the nucleation efficiency of the catalysts studied, which resulted in relatively consistent solder joint undercoolings of ~10 K for 550 µm solder spheres, but the authors demonstrated an alternative method to β-Sn grain orientation control by only allowing a single possible β-Sn orientation to grow via the given orientation relationship between β-Sn and the nucleating catalyst.

In the research presented here we have added pure Ge to the set of inoculating phases for β-Sn. Germanium was chosen as a potential highly potent nucleating phase due to it diamond cubic crystal structure, which has a lattice paraments of 5.66 Å, only differing from the a/b axis of β-Sn by ~3% (a, b = 5.83 Å, c = 3.18 Å). Germanium has a high melting temperature relative to Sn (T_M (Ge) = 938 °C, T_M (Sn) = 232 °C), has low solubility in liquid or solid Sn, and forms a simple binary eutectic with Sn with the eutectic composition at approximately 0.1 at% Ge, indicating the stability of solid Ge in the liquid melt to support Sn nucleation. [22] Additionally, when considering viable solute additions for the growth restriction of Sn, such as Bi or Zn, the creation of a ternary Sn-Bi/Zn-Ge alloy would not interfere with availability of

Bi or Zn in the liquid, as Ge forms simple binary eutectics with both potential solutes, has no solubility of either solute in Ge (or vice versa), and no intermetallics exist in either ternary system. [23], [24] Thus, this study investigates the use of Ge as a potential grain-refining, inoculant phase for β-Sn. The orientation relationships that form between β-Sn and Ge have been examined by solid-state and liquid-state dewetting of pure Sn films on single crystal Ge substrates, inspired by experimental approaches used to analyze orientation relationships in other metallic systems, such as Ag films on polycrystalline Ni substrates. [25], [26]

EXPERIMENTAL PROCEDURES

Pure Sn films were deposited on single crystal, pure Ge substrates of the following orientations: (100), (110), and (111). The Ge single crystal wafers were purchased from MTI Corporation as 1" (2.54 cm) diameter by 500 μm thick wafers, with the planar orientations of the crystals accurate to ± 0.5 °. The surface roughness of the wafers was reported from MTI Corporations at purchase to be < 8 Å. The Ge wafers were scored and cleaved into ~ 3x3 mm substrate samples. Each substrate was then etched in a concentrated hydrofluoric acid (49 % HF) solution to remove any native oxide via the procedure detailed in [27]. The etched substrates were rinsed in deionized water, acetone, and dried in air.

The e-beam deposition of the pure Sn on to the Ge substrates was performed at the National Institute of Standards and Technology (NIST) in Gaithersburg, MD, USA. The Ge substrates were first mounted on a water-cooled rotary stage that permitted the substrates to be aimed toward or away from the deposition sources in a high vacuum chamber with base pressure in the high 10^{-8} torr range. Deposition utilized a three source, 10 kW e-beam evaporation system. One source was used to evaporate Ti prior to the Sn deposition, the substrates were shielded from the Ti source using the rotary stage, in order to accelerate pump down and improve base and operating vacuum levels. A second source contained the Sn in a graphite crucible, toward which the substrates were aimed for deposition. The depositions were performed at a starting vacuum level of 1.5^{-7} torr (2.0^{-8} kPa). Deposition rates varied from approximately 1-2 Å/s, as determined using quartz crystal monitors. The final, as-deposited thickness of the Sn films on the substrate samples was 100 nm, as determined using the quartz crystal monitors. After deposition, the film/substrate samples were removed from the vacuum chamber. The as-deposited samples were examined via scanning electron microscopy (SEM) using a FEI Quanta 3-D Field Emission Dual-beam SEM. Annealing of the film/substrate samples was performed in a Texas Instruments Q2000 differential scanning calorimeter (DSC), calibrated to the melting temperature of pure Indium. The samples were hermetically sealed in Al DSC pans and run under a constant flow of N_2 through the chamber. During solid-state dewetting, 1, 3x3 mm substrate/film sample from each substrate orientation (i.e. 3 film/substrate samples total) was heated to 150 °C at 20 °C/min, isothermally held at 150 °C for 5 mins, and then cooled to room temperature at 20 °C/min. For the liquid-state dewetting, 1, 3x3 mm substrate/film sample from each substrate orientation

(i.e. 3 film/substrate samples total) was heated to 235 °C at 20 °C/min, isothermally held at 235 °C for 1 mins, and then cooled to room temperature at 20 °C/min. Note that the short annealing times were chosen to minimize any potential oxidation of the Sn film during heating. The as-deposited and annealed sample orientations of the Sn films on the Ge substrates were then measured via electron backscatter diffraction (EBSD) by scanning 3 randomly selected scan areas (~ 55 x 35 μm) from each sample using a FEI Teneo Field Emission SEM operating an Oxford Instruments EBSD detector at the Sensitive Instrument Facility located at Ames Laboratory in Ames, IA, USA.

Computational Methods

Density functional theory (DFT) simulations were utilized to quantify relative interfacial binding energies of interfacing Sn/Ge planes and orientations for comparison to the experimental results. Perfect interfaces of Sn and Ge were built using the LAMMPS code [28] and visualized with the Open Visualization Tool (OVITO). [29] Two different interface orientations were created, one of the cube-on-cube orientation, $(001)_{Sn} \parallel (100)_{Ge}$ and $[100]_{Sn} \parallel [100]_{Ge}$, discussed in the introductory motivations, and one of the experimentally observed orientation relationship, $(100)_{Sn} \parallel (111)_{Ge}$ and $[100]_{Sn} \parallel [101]_{Ge}$, discussed in the result section below. The interfacial relaxation was simulated using the Vienna Ab initio Simulation Package (VASP) DFT code. [30], [31] Projector-augmented wave (PAW) pseudopotentials were utilized to replace core electrons [32], [33], and the exchange-correlation was calculated using the generalized gradient approximation proposed by Perdew, Burke, and Ernzerhof (GGA-PBE). [34] For example, in the case on β-Sn, since the electron configuration of Sn is [Kr] 4d10 5s2 5p2, then 14 electrons were treated as valence electrons, that is 4d10 5s2 5p2. The rest of the electrons were then treated as core electrons and their wave functions treated as an "effective wave function" with PAW pseudopotentials. For relaxation of the film interfaces, a 4x4x1 K-mesh was constructed, along with a 10x10x1 mesh for the energy calculations. The plane waves were expanded to a kinetic energy cutoff of 600 eV. Self-consistent field (SCF) iterations were stopped when a tolerance on energy difference of $1x10^{-6}$ eV was reached, and the ionic relaxation stopped when forces on all atoms fell below 0.01 eV/Å. The interfaces were created as slabs with periodic boundary conditions with a vacuum layer of 25 Å perpendicular to the interface to avoid interaction between adjacent layers. The Ge free surface was hydrogen passivated (sp^3) to avoid fictitious surface charges and the bottom 3-4 atomic layers of Ge were kept fixed at their bulk atomic coordinates to simulate the substrate. All Sn atoms were free to fully relax.

RESULTS AND DISCUSSION

Grain morphologies and orientations were characterized using SEM and EBSD from the as-deposited films, and the solid- and liquid-state annealed samples, and are discussed sequentially based on the three annealing treatments It is important to note that all SEM and EBSD scan areas were randomly selected to

provide multiple independent observations for each condition, i.e. no areas were tracked from the as-deposited state to after solid-state annealing or after liquid-state annealing. Finally, results from the DFT simulations of Ge/Sn interfaces are discussed and compared to the observed experimental results.

As-deposited Sn film/Ge substrate samples

The as-deposited Sn films formed partially wetted, polycrystalline films, as seen in Figures 1 a-c, on the Ge (100), (110), and (111) substrate orientations, respectively. It was apparent from the SEM observations that the films were not dense in the as-deposited state; interconnected Sn grains were observed. The as-deposited Sn films displayed a consistent dominant (001) Sn c-axis texture (parallel to the z-axis sample direction, i.e. normal to the film surface), with various, random orientations in the x- and y-axis sample directions. This consistent z-axis texture of the Sn films on each Ge substrate orientation is displayed in the EBSD scans shown in Figure 2 a-i. Given the consistency of the z-axis as-deposited film texture, which was indifferent to the underlying Ge substrate orientation, (and the variations seen in the x- and y-planes) it is likely that this was determined by deposition kinetics during the physical vapor deposition process.

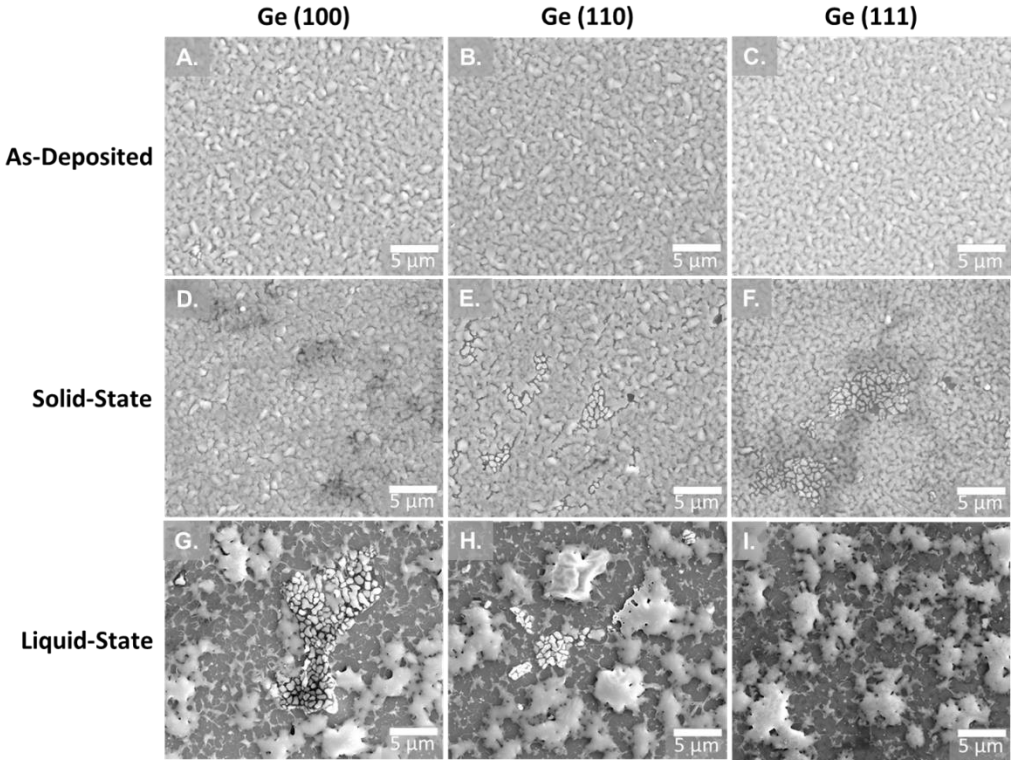

Figure 1 Representative micrographs of the (a-c) as-deposited, partially dense Sn films on the (a) Ge (100), (b) Ge (110), and (c) Ge (111) substrates, (d-f) solid-state annealed, partial dense and partially dewetted Sn films on the (d) Ge (100), (e) Ge (110), and (f) Ge (111) substrates, and (g-i) liquid-state annealed, fully dewetted and partially dewetted Sn films on the (g) Ge (100), (h) Ge (110), and (i) Ge (111) substrates.

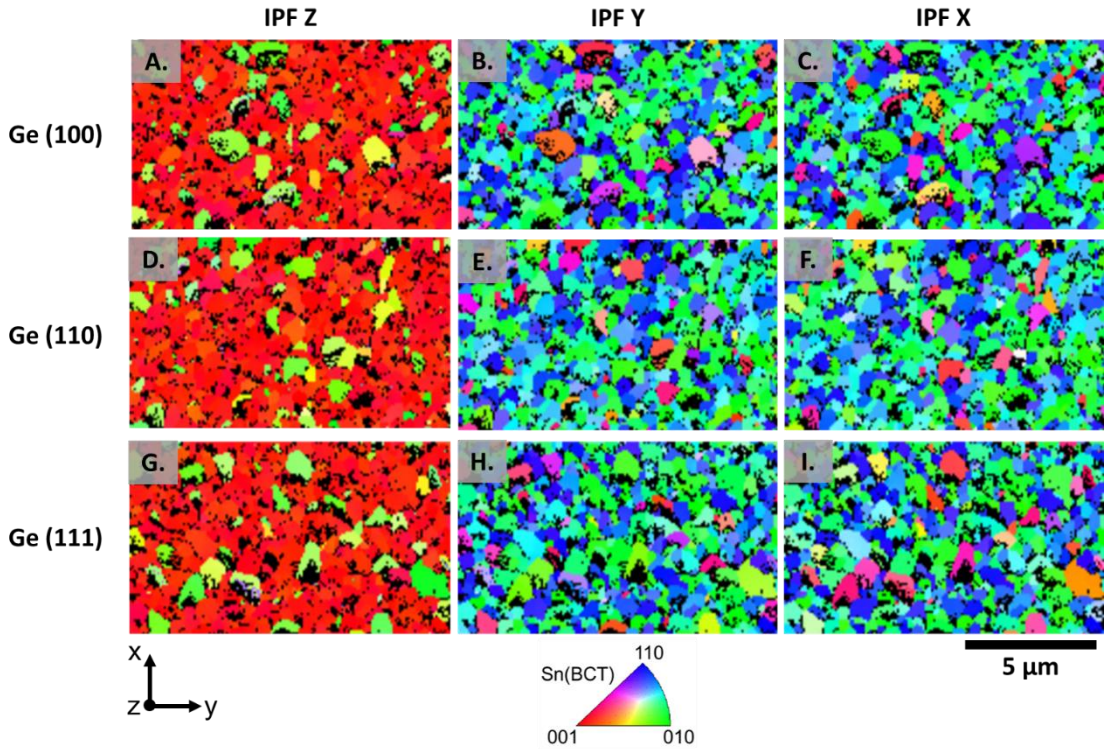

Figure 2 Representative EBSD inverse pole figure (IPF) color maps in the z-, y-, and x-axis sample frame orientations (as labeled). The IPF maps represent a single scan area of the as-deposited Sn films on the (a-c) Ge (100), (d-f) Ge (110), and (g-i) Ge (111) substrates. The Sn films displayed the same film texture regardless of the underlying Ge substrate orientation. (The scale bar has been calibrated to apply to each scan image).

Solid-state annealed film/substrate samples

During solid-state annealing, the samples were held at 150 °C (65% of the Sn melting temperature) for 5 min. The morphologies of the Sn films on their respective Ge single crystal substrates remained unchanged from the initial as-deposited state. The films largely maintained their partially wetted, polycrystalline structure (Figure 1 d-f). In some instances, small areas of dewetting were noted, as in Figure 1 e and f. The EBSD measurements from the solid-state annealed samples also displayed little change from the as-deposited state. As can be seen in Figure 3 a-i, the solid-state annealed Sn films largely maintained the (001), c-axis Sn texture in the z-axis sample direction, with various orientations of Sn in the directions parallel to the x- and y-axis sample directions. Although the short time and lower temperature of the solid-state anneal was chosen to avoid significant oxidation of the Sn film during the DSC experiments, when the procedure did not result in any significant dewetting, samples were annealed up to 210 °C – 90.5 % of the Sn melting temperature – for as long as 12hrs in a tube furnace under a reducing, Ar+5%H, atmosphere, but all of the applied treatments resulted in the same outcome as the presented samples in Figures 1 d-f and Figure 3 a-i. We believe the absence of dewetting in the solid state was likely due to the native SnO_2 layer

that initially formed on first exposure to air. Future solid-state annealing experiments would benefit from a combined oxide etching and vacuum annealing set up, where an ultra-high vacuum chamber, ion etching system, and furnace or heating stage, would be utilized to remove the SnO_2 layer and immediately perform the annealing treatments without breaking vacuum. Similar techniques have been successfully employed in the case of the solid-state dewetting of pure Cu films on sapphire substrates. [35]

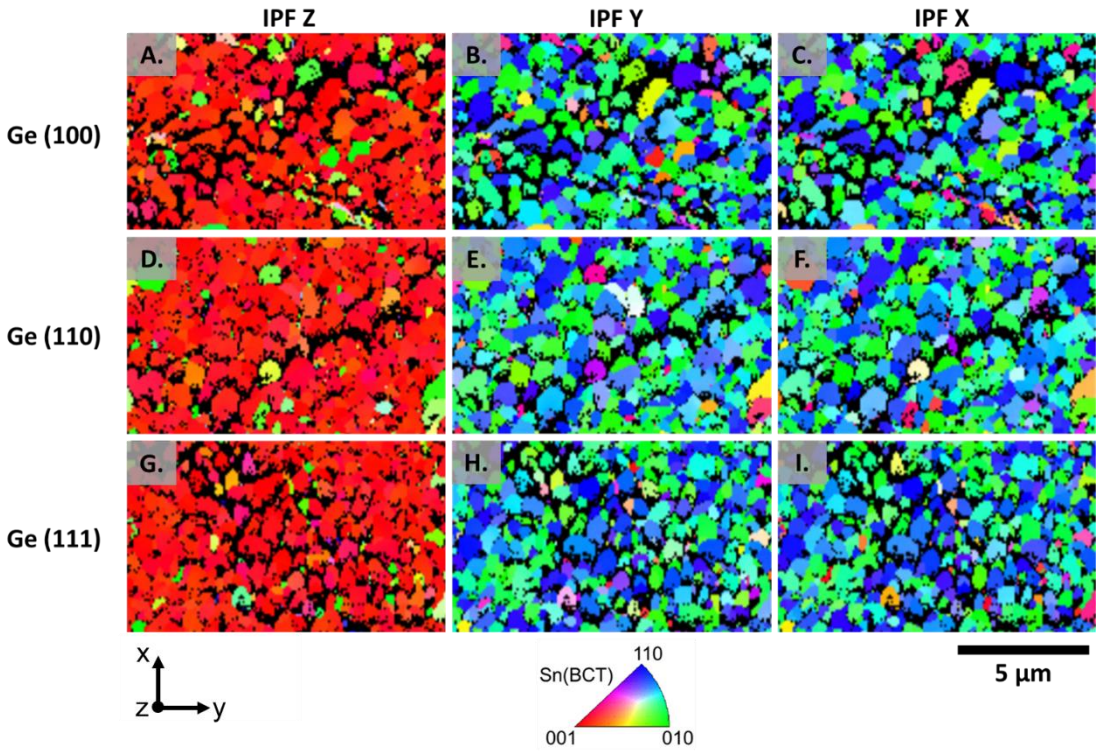

Figure 3 Representative EBSD inverse pole figure (IPF) color maps in the z-, y-, and x-axis sample frame orientations (as labeled). The IPF maps represent a single scan area of the solid-state annealed Sn films on the (a-c) Ge (100), (d-f) Ge (110), and (g-i) Ge (111) substrates. The Sn films displayed the same film texture regardless of the underlying Ge substrate orientation. (The scale bar has been calibrated to apply to each scan image).

Liquid-state annealed film substrate samples

Large-scale dewetting of the Sn films on the Ge substrates and grain reorientation were observed after liquid-state annealing at 235 °C (Sn T_M = 232 °C) for 1 min and solidification. As can be seen in Figure 1 g-i, the Sn films dewet, forming Sn islands that were commonly linked by small, "spider-web" tendrils of Sn branching out from each of the islands. This resulted in a partially interconnected network of the dewetted Sn, as shown in Figure 1 g-i. There were also areas where only partial dewetting had occurred (Figure 1 g and h). It is likely that this partial dewetting was a result of incomplete melting of the Sn film in those areas, as the liquid-state anneal was only 235 °C for 1 min. to avoid excessive oxidation of the Sn. This short time above the Sn melting temperature likely did not allow for complete melting of the Sn films,

resulting in some small areas of only partial dewetting. It is important to note that the dewetting morphology of the Sn films across all the examined substrate orientations was highly consistent. All the samples expressed similar morphological characteristics of interconnected, tendril-like droplets as well as isolated areas of only partial dewetting.

Upon EBSD examination after liquid-state dewetting, it became apparent that the orientations of the re-solidified Sn films on the Ge substrates had changed from the as-deposited c-axis texture, with varying results depending on the underlying Ge substrate orientation. In the Ge (100) and (110) substrate samples, a large variety of Sn orientations were observed in the liquid-state dewet samples. The randomly selected scan areas for the Ge (100) substrate did display isolated areas of consistent plane (z-axis) and directional (x- and y-axes) alignment. For example, scan areas 2 and 3 shown in Figure 4 both show areas where the $(110)_{Sn}$ is parallel to the z-axis (i.e. the blue on red areas in IPF z) with the $[001]_{Sn}$ parallel to the y-axis and the $[110]_{Sn}$ parallel to the x-axis, but the variety of different orientation relationships displayed across the sample also signals to a lack of a dominant orientation relationship between the re-solidified Sn droplets and the Ge (100) substrate. The Ge (110) substrates orientations, shown in Figure 5, expressed even less consistency in the directional, x- and y-axes, orientations than those measured for the Ge (100) substrate. Overall, the Ge (100) and (110) liquid-annealed substrates did not produce Sn orientations that appeared to be dictated strongly by the underlying Ge substrate orientation. This variability in Sn grain orientation signals a lack of a dominant orientation relationship between the re-solidified Sn and the Ge (100) and (110) substrate orientations. Detailed IPF maps exemplifying the range of Sn orientations expressed in the Ge (100) and Ge (110) samples is shown in Figure S1 in the supplemental figures. If a strong orientation relationship did exist, it is likely that a single Sn orientation, or sub-group of orientations, with consistent alignment across all sample frame orientations, would dominate the observed re-solidified Sn orientations given the single crystal nature of the substrates. This was not fully the case in the Ge (100) substrate, and particularly was not true for the (110) substrate samples examined here. Thus, it was concluded that, at the very least, pure Sn lacks a strongly preferred orientation relationship with the (100) or (110) planar orientations of pure Ge.

It should be noted here that despite the annealing of the samples in the DSC, undercooling measurements from the individual film/substrate samples could not be accurately measured due to the small volume of Sn on the ~3x3 mm substrates (with a Sn deposition thickness of 100 nm). This was an approximate Sn volume of $9x10^{-7}$ cm^3, or, approximately $6.6x10^{-6}$ g ($6.6x10^{-3}$ mg) of pure Sn (the density of pure Sn being 7.3 g/cm^3). That is also not including within these estimated numbers the unknown volume of Sn having oxidized after deposition and during the annealing process. Thus, unfortunately, the Sn signal

in the resulting DSC experiments was too low to provide accurate undercooling measurements for the liquid-state annealed samples in the current study.

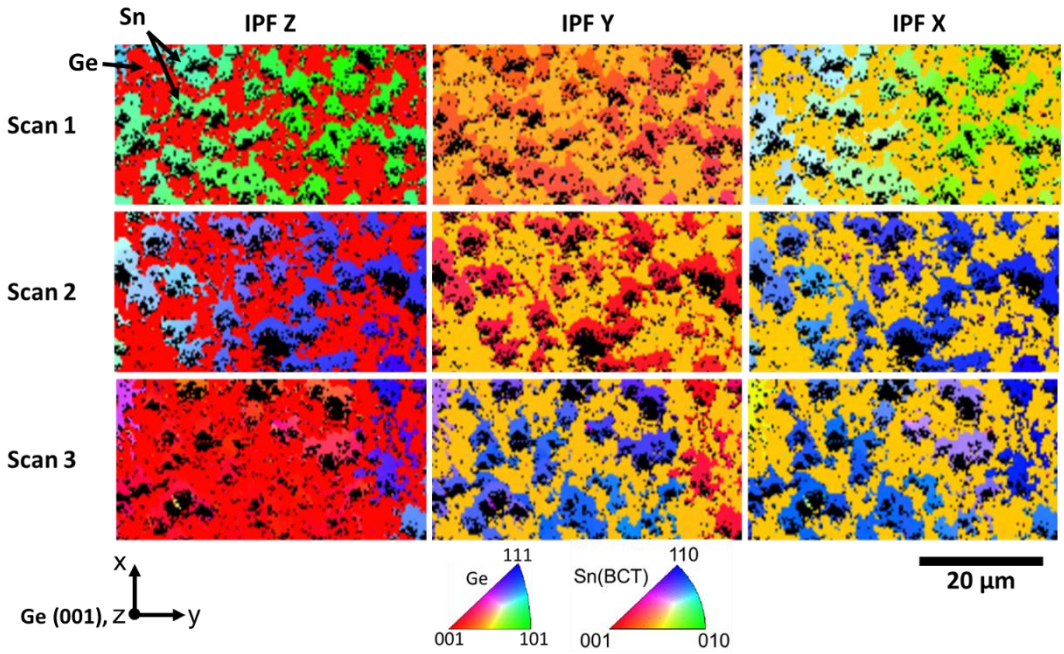

Figure 4 EBSD inverse pole figure (IPF) color maps in the z-, y-, and x-axis sample frame orientations (as labeled) from the three independent scan areas examined for the liquid-state annealed Ge (100) substrate sample. The IPF maps display both the underlying Ge orientation, as well as the orientations of the dewet Sn droplets on the Ge (see phase labels, top left corner). The Sn droplets displayed a range of orientations, but with consistency noted between z-axis orientations and directional, x- and y-axis orientations. (The scale bar has been calibrated to apply to each scan image).

The Sn films on the Ge (111) single crystal substrates consistently dewet during liquid state annealing and re-solidified with the following orientation relationship (Figure 6):

$$(100)_{Sn} \parallel (111)_{Ge} \text{ and } [100]_{Sn} \parallel [110]_{Ge}$$

As seen in Figure 6, the z-axis direction of the film in the EBSD inverse pole figure map is parallel to the Sn a/b-axis direction in each scan area. Additionally, the x-axis and y-axis directions are also oriented in each observed sample area, indicating that the Sn crystal is not only aligning parallel plane interfaces with the Ge substrate, but also parallel directions within those planes, resulting in the observed orientation relationship between the two crystals. A detailed IPF map exemplifying the oriented nature of the dewetted Sn from the Ge (111) sample is shown in Figure S1 in the supplemental figures. It is important to note here that the orientation of the Ge crystal in the x-axis sample direction in Figure 6 should reflect the direction perpendicular to the Ge <101>, i.e. the <112>, but the direction reflected in the collected scans displays a direction closer to a <123>-type direction. This result does not agree with the Ge orientations depicted in

the z- and y-axis sample directions in the collected scan, and currently, the reason for this discrepancy in the experimental data is unknown. Although, it could potentially be due to poor calibration of the EBSD system, itself, on which the data was collected.

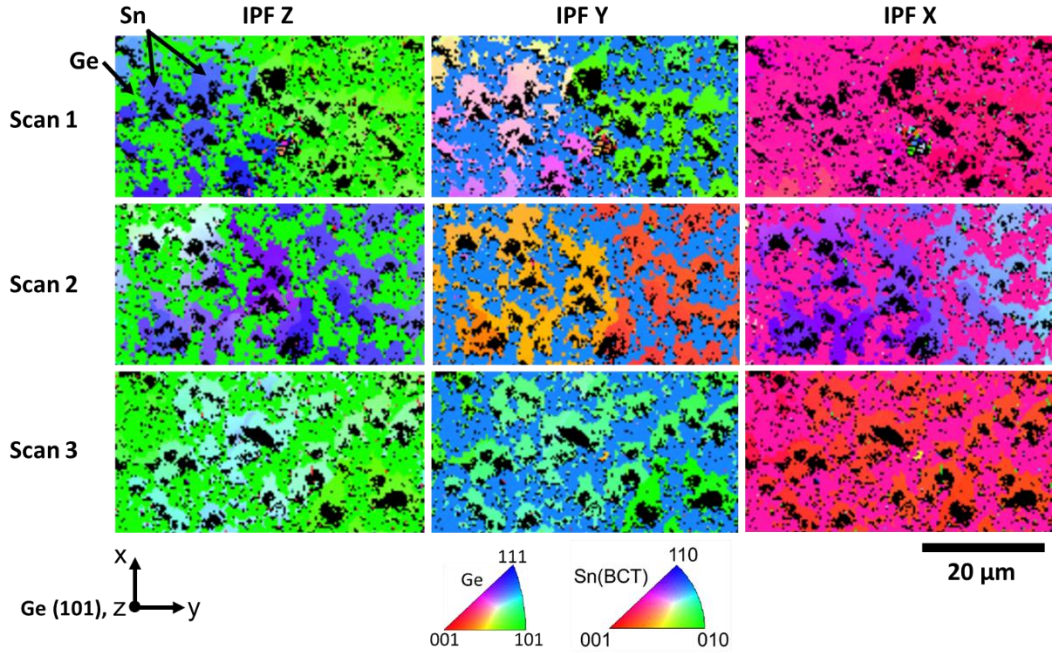

Figure 5 EBSD inverse pole figure (IPF) color maps in the z-, y-, and x-axis sample frame orientations (as labeled) from the three independent scan areas examined for the liquid-state annealed Ge (110) substrate sample. The IPF maps display both the underlying Ge orientation, as well as the orientations of the dewet Sn droplets on the Ge (see phase labels, top left corner). The Sn droplets displayed a range of orientations and seem to be largely, uninfluenced by the underlying Ge substrate orientation. (The scale bar has been calibrated to apply to each scan image).

If this observed orientation relationship is examined from an atom-matching perspective, as seen in Figure 7, the Sn atoms and Ge atoms within the respective (100) and (111) planes do not match up perfectly. If the center atoms in the Figure 7 are used as an origin, significant strain would have to be imposed on either crystal to allow for full atomic alignment of the Sn and Ge atoms. It is possible though, that the two crystals form a partial orientation relationship based on coincident site lattice (CSL) matching. It can be seen in Figure 7 that the corner atoms and the central atoms (highlighted by the dashed lines) of the graphed Sn and Ge lattices match closer than the other surrounding atomic sites. In fact, this repeating, “kite”-like, structure is similar to the CSL formation for Σ3-type boundaries, which can occur along the <112> twinning direction in face-centered cubic (FCC) materials (this potential Sn/Ge CSL is also along a [112]-type direction). [36] Another important observation from this data, was the consistency and singularity of the experimentally observed orientation relationship. Germanium, itself, has 3-fold symmetry on the (111)

plane, thus, one would expect to observe three different orientation variants on the (111) plane if a true orientation were to exist, but the experimental samples only produced a single orientation, as seen from the data. This could potentially be due to the influence of Ge substrate structures (discussed more below), the influence of a CSL-type relationship instead of a direct relationship with the Ge (111), or the potential that, given the interconnected nature of the liquid-state dewet Sn film morphology, that the Sn film re-solidified as a single grain, thus providing the single observed orientation – although, there was no way to detect if this was actually the case in the current experimental set up, and it is important to remember that all of the liquid-state annealed samples displayed these same interconnect, tendril-like morphologies.

If the atom-matching results from these Sn/Ge samples are compared to phases that are known to be highly potent nucleants of β-Sn, where, for example the orientation relationships between β-Sn and $NiSn_4$, $PtSn_4$, and $PdSn_4$ IMC (XSn_4-type, stannide IMC) were studied [19], [21], the differences between the highly potent XSn_4/β-Sn orientation relationship and the Ge/β-Sn orientation relationship become apparent. In the case of XSn_4-type IMC, the orientation relationships were defined as the following:

$$(008)XSn_4 \parallel (100)Sn \; and \; [100]XSn_4 \parallel [001]Sn$$

In both the XSn_4 IMC and the Ge cases, it was the β-Sn (100) plane – the close-packed plane of β-Sn – that was utilized in the orientation relationship. The major difference between these different systems though, was the prevalence of Sn atoms in the XSn_4 IMC structures. In particular, the (008) plane of the XSn_4 IMC is not only the close-packed plane of the crystal, but it also consists entirely of Sn atoms, and the d-spacing of the (008) plane (the spacing between parallel (008)-type crystal planes) is ~0.28-0.29 nm, while the d-spacing in β-Sn (100)-type planes is ~0.29 nm – matching almost exactly. Both the (008) XSn_4 plane and the (100) β-Sn plane involve zig-zag rows of Sn atoms, along the [100] and [010] directions in XSn_4 and along the [100] direction in β-Sn. These interfacing planes of zig-zag Sn atoms have a mismatch of 9-12 % in the varying XSn_4 crystals, and the low d-spacing mismatch (0.3-0.6 %) between the crystals results in a very good fit of every other β-Sn row at the interface, giving rise to the β-Sn nucleation potency of these XSn_4-type IMC. [21]

In the case of the Ge/β-Sn OR observed here, the d-spacing of the Ge (111) planes is ~0.33 nm, differing from the (100)-type planes of the β-Sn by ~14%. Additionally, the Ge atom spacing in the (111) Ge plane is ~0.40 nm, while the Sn atom spacing in the (100) Sn plane is ~0.29 nm, a mismatch of ~37%. Overall, the atomic matching in β-Sn (100) and Ge (111), while consistently observed in the experimental sample examined here, does not appear to provide a beneficial template for nucleation without considerable strain imposed to either lattice. If the potential for a Σ3-type CSL relationship is accounted for, the matching of the Sn/Ge atoms in that orientation does provide a closer match. For examples, the corner atoms in Figure 7 differ in the x-axis direction by only ~3%, and the central atoms only differ in the y-axis direction by

~10%. This close atomic match and the potential for such a CSL-type orientation relationship between Sn and Ge is, thus, an important topic of study for future work in understanding the relationships between these two elements. The experimentally observed orientation relationship, as well as the Sn/Ge lattice parameter matching, cube-on-cube orientation, (an atomic mismatch of only ~3%) that initially prompted this study of Ge as an inoculant for Sn, were analyzed more closely in the following section where DFT simulations were utilized to measure the interfacial binding energy of both sets of orientations.

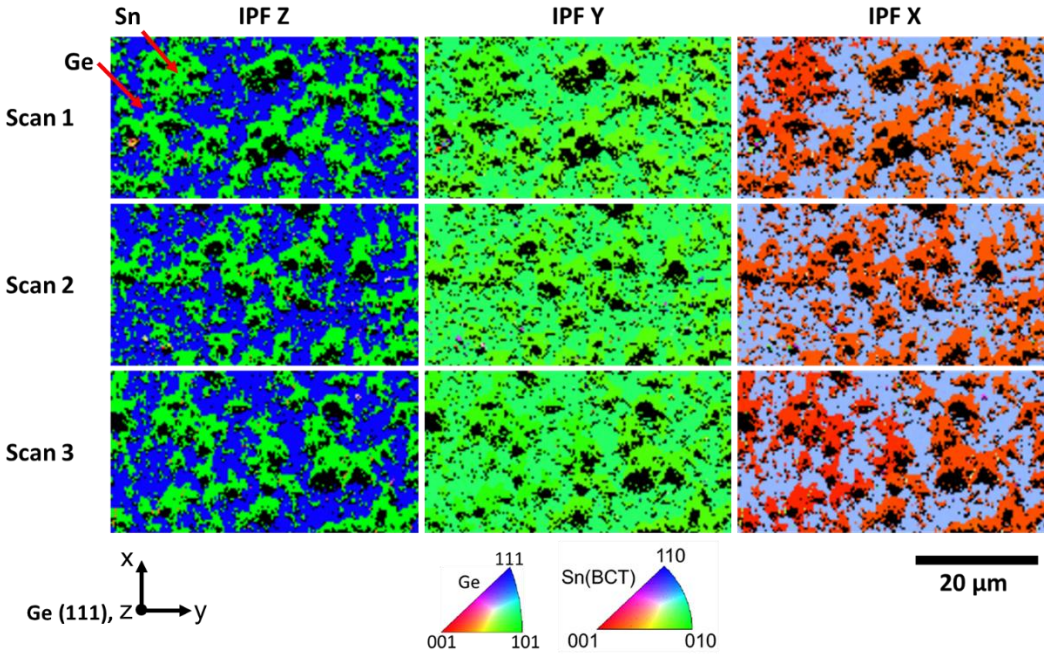

Figure 6 EBSD inverse pole figure (IPF) color maps in the z-, y-, and x-axis sample frame orientations (as labeled) from the three independent scan areas examined for the liquid-state annealed Ge (111) substrate sample. The IPF maps display both the underlying Ge orientation, as well as the orientations of the dewet Sn droplets on the Ge (see phase labels, top left corner). The Sn droplets display a single orientation, consistent across each sample area and in each sample direction. (The scale bar has been calibrated to apply to each scan image).

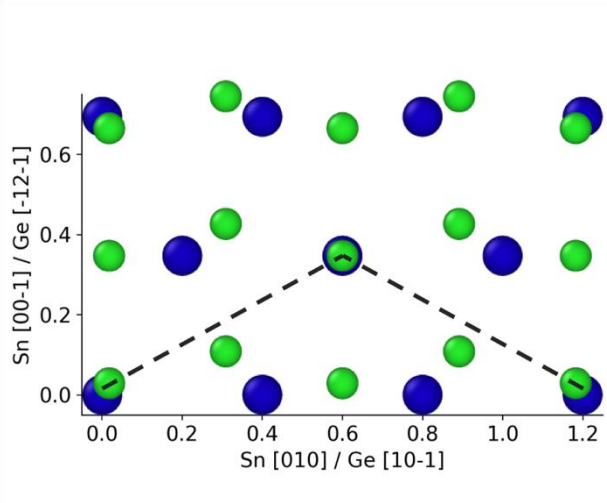

Figure 7 A graph displaying the unstrained, equilibrium, experimental atomic spacing for single planes of Sn (100) and Ge (111) planes, with alignment along the Sn [010] and Ge [10-1] directions, i.e. the orientation relationship exemplified by the liquid-state annealed Ge (111) substrate sample. With two central atoms set to overlap, one can compare the atomic matching of the two planes. Ge atoms are shown in blue and Sn atoms in green; Sn atoms are smaller only to show overlap with Ge. The black dashed lines indicate the potential CSL-type matching relationship between the corner and center atoms.

Sn/Ge interfaces via DFT simulations

Simulations using DFT were employed to analyze the observed orientation relationship identified in the Ge (111) substrate sample and compare it with the cube-on-cube orientation that originally motivated this work and that was observed in some instances on the Ge (100) substrate sample (Figure 4, scan 1). Interfacial binding energies were calculated from these simulations to offer a better understanding of the ideal interface matching between Sn and Ge.

Figure 8 shows the constructed interfaces from the top and side view prior to relaxation. Figure 9 displays the top view of the relaxed interfaces. Visually, the cube-on-cube orientation relationship that prompted this study of Ge and Sn appears to have a more ideal atomic match as compared to the experimentally observed orientation relationship, as previously discussed, with the corner atoms of the (001) Sn overlapping with the (100) corner atoms of the Ge. Table 1 shows the simulated interface orientations, the number of atoms per simulation, the interfacial area per simulation, the calculated interfacial binding energies of the relaxed structures on a per atom basis, and the calculated interfacial binding energies of the relaxed structures on a per area basis. These interfacial binding energies were calculated with respect to the sum energies of the separate (non-interfacing) Ge and Sn slabs. The value of this interfacial binding energy per atom, E_b, was calculated via Equation 2 below,

$$E_b = \frac{1}{N}\left[E_{Ge/Sn} - (E_{Ge} + E_{Sn})\right] \quad (2)$$

where N is the total number of atoms in the simulation, $E_{Ge/Sn}$ is the total energy of the Ge slab interfacing with the Sn slab in the chosen orientations, E_{Ge} is the total energy of the isolated Ge slab of a chosen orientation, and E_{Sn} is the total energy of the isolated Sn slab of a chosen orientation. The value of this interfacial binding energy per area, γ_b, was then simply calculated directly from the interfacial binding energy per atom, E_b, by multiplying by the atoms/area of each simulation. Based on Equation 2, the negative signs of the calculated interfacial binding energies highlight the large magnitude of the summed energies of the Ge and Sn isolated slabs as compared to the total energy of the Ge/Sn interface system. Overall this indicates a reduction of energy in the system through the elimination of a single Ge free surface and a single Sn free surface during the creation of the Ge/Sn interface. Further, the larger the magnitude of this negative interfacial binding energy, the lower the total energy of the Ge/Sn interface system, $E_{Ge/Sn}$, and thus, the lower the energy of the Ge/Sn interface, itself. This means that a larger negative value for the interfacial binding energy indicates the preferred formation of a given interface orientation.

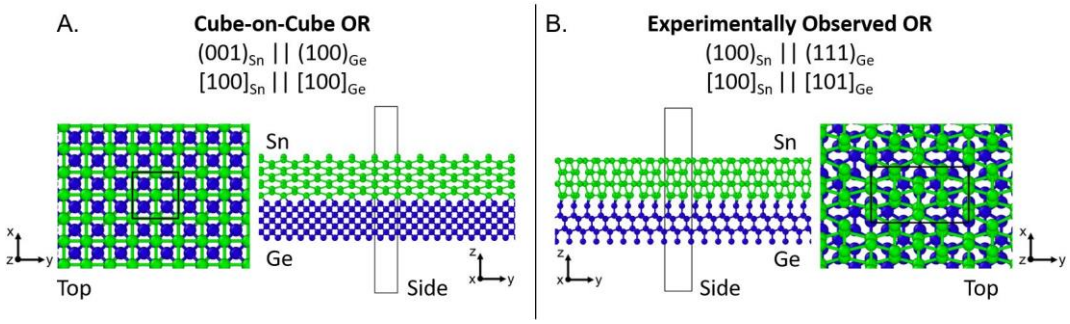

Figure 8 Top and side views of the un-relaxed film/substrate structures of (a.) the cube-on-cube orientation and (b.) the experimentally observed orientation relationship. The Sn atoms are colored green and the Ge atoms are colored blue; periodic replicas are shown in the x/y directions, with the simulation cell as a black box. Hydrogen passivation of the Ge free surface not shown.

On a per-atom basis, the interfacial binding energy, E_b, of the cube-on-cube orientation was calculated to be -0.13 eV/atom. Similarly, the interfacial binding energy per area, γ_b, of the cube-on-cube orientation was calculated to be -1.7 J/m^2. In comparison, the interfacial binding energy per atom, E_b, of the experimentally observed orientation relationship was calculated to be -0.11 eV/atom, with an interfacial binding energy per area, γ_b, of -1.4 J/m^2. Thus, the slightly more negative interfacial binding energy values of the cube-on-cube orientation indicate a preference for formation of the cube-on-cube orientation over that of the experimentally observed orientation relationship. When considering the binding energies on a per area basis, the cube-on-cube orientation is still slightly preferred over the experimentally observed orientation relationship, despite the increased atomic density of the close-packed planes involved in the

experimentally observed orientation relationship. Overall, the magnitudes of the simulated values are comparable.

Table 1 The simulated interface orientations, the number of atoms per simulation (*N*), the interfacial area per simulation, the calculated interfacial binding energies of the relaxed structures on a per atom basis, and the calculated interfacial binding energies of the relaxed structures on a per atom basis (E_b), and the calculated interfacial binding energies of the relaxed structures on a per area basis (γ_b).

OR	**Parallel Planes**	**Parallel Directions**	**Number of Atoms, *N***	**Simulated Area (Å^2)**	***Eb* (eV/atom)**	**γ_b (J/m^2)**
Cube-on-Cube	Ge (100), Sn (001)	Ge [100], Sn [100]	27	33.2	-0.13	-1.7
Experimentally Observed	Ge (111), Sn (100)	Ge [101], Sn [100]	68	85.1	-0.11	-1.4

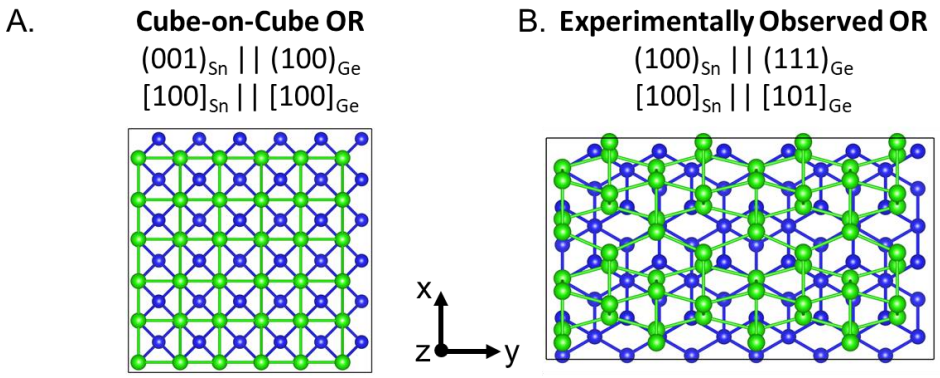

Figure 9 Top views of the fully relaxed film/substrate model structures of (a.) the cube-on-cube orientation and (b.) the experimentally observed orientation relationship. The Sn atoms are colored green and the Ge atoms are colored blue.

These simulation results do not provide a clear explanation for the observed experimental results, in which the orientation relationship, Ge (111) || Sn (100) and Ge [101] || Sn [100], was the only consistent Sn film texture for any Ge single crystal orientation. Since atomic-scale, geometry-based matching of the cube-on-cube orientation originally prompted this investigation into Ge/Sn orientation relationships, it is not a surprising result that the cube-on-cube orientation, Ge (100) || Sn (001) and Ge [100] || Sn [100], had a slightly lower relative interfacial binding energy than the more observed orientation relationship. Overall, both Sn/Ge interfaces showed strong binding, on the same order as Ge liquid on various orientations of Ge single crystals [37], with large differences between the two calculated perfect systems.

As discussed previously, it is possible that the observed orientation relationship could be attributed to a semi-coherent interface relationship, such as a CSL dislocation structure, but it is also possible that the (111) Ge interface with Sn could have become non-planar during annealing and dewetting, forming, such as surface steps, kinks, or facets. In fact, Figure 1 shows that some surface roughening of the Ge single crystal surfaces has occurred between the dewetted patches of the liquid phase annealed samples. Since such structures occur on the atomic scale at the vapor/solid interface, these structures would not be apparent from the imaging scale of EBSD measurements and would still result in a Ge (111) identification of the substrate. Additional research could be performed to analyze the Sn/Ge interface planes before and after annealing and whether steps, kinks, or facets could be influencing film texture, as in similar studies in other systems. [35] Additionally, further DFT simulations should be performed to compare interfacial binding energies once the Sn/Ge interface structures for all three Ge orientation have been determined. Finally, a wider survey of orientations and misorientations in the Sn/Ge system using DFT, while outside the scope of the work reported here, may also yield useful results. Finally, experiments and DFT simulations of the ultimate system of interest – facetted Ge particles in a Sn liquid matrix – are needed to characterize the ability of Ge surfaces to catalyze nucleation. Note however, that those systems would require a lower fidelity model, e.g. classical molecular dynamics, due to computational restrictions on size for DFT.

CONCLUSIONS

The morphologies and orientations of as-deposited, solid-state annealed, and liquid-state annealed pure Sn films on single crystal Ge (100), (110), and (111) substrates were analyzed in this work. The goal of this study was to identify whether Sn/Ge orientation relationships indicate the potential of Ge as a heterogeneous nucleant for Sn which along with other inoculation additives and growth-restricting solutes, such as Bi or Zn, could lead to grain size refinement. The texture results obtained with EBSD were compared with DFT calculations of binding energies of relaxed Sn/Ge interface structures. The following conclusion were made based on the experimental and simulation results:

1. The as-deposited Sn films all deposited with a Sn (001) || z-axis texture, regardless of the underlying Ge substrates orientation.
2. Solid state annealing at 150 °C for 5 min did not result in any significant dewetting of the Sn films, and the films maintained their as-deposited texture of Sn (001) || z-axis, regardless of the underlying Ge substrate orientation.
3. Liquid-state annealing at 235 °C for 1 min resulted is large-scale dewetting of the Sn films and re-orientation of the Sn grains after solidification on all three Ge substrate orientations. The dewetted Sn grains on all samples were largely isolated particles with tendrils of Sn appearing to link some of the droplets.

4. The Ge (100) and (110) single crystal substrates, although displaying regions of dewetted Sn grains with common orientations, did not produce re-solidified Sn films with any dominant film texture after liquid-state annealing that could be related to the underlying Ge substrate orientations.
5. The Ge (111) single crystal substrate showed a single Sn/Ge orientation relationship identified as:

$$(100)_{Sn} \parallel (111)_{Ge} \text{ and } [100]_{Sn} \parallel [110]_{Ge}$$

6. DFT simulations of the experimentally observed Ge (111) sample orientation relationship and the Ge/Sn cube-on-cube orientation relationship predicted that the favorable formation of both orientations based on the simulated relative interfacial binding energies of the two interfaces.

A key observation of this work was the reproducibility of the Sn/Ge (111) substrate orientation relationship. Given the data collected here it is currently unclear if this highly consistent orientation relationship can be solely attributed to Ge (111) substrate lattice orientation alone or if Ge (111) atomic-level surface structures could be contributing to the results. These measurements were not performed in the current study. Atomic-level interface structure analysis and DFT simulations based on those results could be helpful in quantifying the potential of various Ge surface orientations to nucleate Sn. Based on the results presented here, the addition of faceted Ge particles with (111) bounded surfaces has the potential to promote Sn nucleation in Sn-based solder alloys if this observed orientation relationship also translates to reductions in β-Sn undercooling. Additionally, Sn-based ternary alloy systems employing Ge as an inoculation additive, along with Bi or Zn solutes to promote growth restriction, could be developed to enhance the nucleation of Sn and refine the β-Sn grain size in Sn-based solder alloys for use in microelectronics.

ACKNOWLEDGMENTS

The authors are grateful for Dan Josell and Maureen Williams at NIST for their assistance in performing the Sn film depositions, to Qingfeng Xing, Matt Lynn, Matt Besser, Mark Clarridge, Sarah Wiley, Emma White, Stephanie Choquette, and Iver Anderson of Ames Laboratory for their help in providing access and training on the EBSD system located at the Sensitive Instrument Facility in Ames, IA, USA, and to David Guzman, formerly at Purdue University and currently at Brookhaven National Laboratory, for his assistance in running the DFT simulations. This work was prepared by Lawrence Livermore National Laboratory (LLNL) under Contract DE-AC52-07NA27344. Ames Laboratory (US-DOE), Purdue University, and Nihon Superior supported this work through Ames Lab Contract No.DE-AC02-07CH11358. Additional funding was provided through government support under and awarded by

the DoD Air Force Office of Scientific Research, National Defense Science and Engineering Graduate (NDSEG) Fellowship, 32 CFR 168a.

REFERENCES

[1] T. R. Bieler, H. Jiang, L. P. Lehman, T. Kirkpatrick, E. J. Cotts, and B. Nandagopal, *IEEE Trans. Compon. Packag. Technol.*, vol. 31, no. 2, pp. 370, 2008.
[2] D. Swenson, *J. Electron. Mater.*, vol. 18, no. 1–3, pp. 39, 2007.
[3] Y.-C. Huang, S.-W. Chen, and K.-S. Wu, *J. Electron. Mater.*, vol. 39, no. 1, pp. 109, 2010.
[4] B. Vonnegut, *J. Colloid Sci.*, vol. 3, pp. 563, 1948.
[5] G. M. Pound and V. K. La Mer, *J. Am. Chem. Soc.*, vol. 74, pp. 2323, 1952.
[6] D. Turnbull and R. E. Cech, *J. Appl. Phys.*, vol. 21, no. 8, p. 804, 1950.
[7] D. Turnbull, vol. 18, no. 5, p. 768, 1950.
[8] D. Turnbull, *J. Chem. Phys.*, vol. 18, no. 5, p. 769, 1950.
[9] J. H. Perepezko, *Mater. Sci. Eng.*, vol. 65, no. 1, pp. 125, 1984.
[10] J. H. Perepezko, *Mater. Sci. Eng. A*, vol. 226–228, pp. 374, 1997.
[11] J. H. Perepezko and G. Wilde, *Curr. Opin. Solid State Mater. Sci.*, vol. 20, no. 1, pp. 3, 2016.
[12] L. P. Lehman, Y. Xing, T. R. Bieler, and E. J. Cotts, *Acta Mater.*, vol. 58, no. 10, pp. 3546, 2010.
[13] K. N. Reeve and C. A. Handwerker, *J. Electron. Mater.*, vol. 47, no. 1, pp. 61, 2018.
[14] T.-K. Lee, T. R. Bieler, C.-U. Kim, and H. Ma, *Fundamentals of Lead-Free Solder Interconnect Technology*. Boston, MA: Springer US, 2015.
[15] M. A. Easton, M. Qian, A. Prasad, and D. H. StJohn, *Curr. Opin. Solid State Mater. Sci.*, vol. 20, no. 1, pp. 13, 2015.
[16] K. N. Reeve, J. R. Holaday, S. M. Choquette, I. E. Anderson, and C. A. Handwerker, *J. Phase Equilibria Diffus.*, vol. 37, no. 4, pp. 369, 2016.
[17] H. Shang, Z. L. Ma, S. A. Belyakov, and C. M. Gourlay, *J. Alloys Compd.*, vol. 715, pp. 471, 2017.
[18] D. H. StJohn, A. Prasad, M. A. Easton, and M. Qian, *Metall. Mater. Trans. A*, vol. 46, no. 11, pp. 4868, 2015.
[19] Z. A. Ma, S. A. Belyakov, T. Nishimura, T. Nishimura, and C. M. Gourlay, *Nat. Commun.*, vol. 8, no. 1916, pp. 1, 2017.
[20] Z. L. Ma, S. A. Belyakov, and C. M. Gourlay, *J. Alloys Compd.*, vol. 682, pp. 326, 2016.
[21] S. A. Belyakov and C. M. Gourlay, *Acta Mater.*, vol. 71, pp. 56, 2014.
[22] R. W. Olesinski and G. J. Abbaschian, *Bull. Alloy Phase Diagr.*, vol. 5, no. 3, pp. 265, 1984.
[23] R. W. Olesinski and G. J. Abbaschian, *Bull. Alloy Phase Diagr.*, vol. 7, no. 6, pp. 535, 1986.
[24] R. W. Olesinski and G. J. Abbaschian, *Bull. Alloy Phase Diagr.*, vol. 6, no. 6, pp. 540, 1985.
[25] P. Wynblatt and D. Chatain, *J. Mater. Sci.*, vol. 50, no. 15, pp. 5262, 2015.
[26] D. Chatain, P. Wynblatt, A. D. Rollett, and G. S. Rohrer, *J. Mater. Sci.*, vol. 50, no. 15, pp. 5276, 2015.
[27] T. Deegan and G. Hughes, *Appl. Surf. Sci.*, vol. 123–124, pp. 66, 1998.
[28] S. Plimpton, *J. Comput. Phys.*, vol. 117, no. 1, pp. 1, 1995.
[29] A. Stukowski, *Model. Simul. Mater. Sci. Eng.*, vol. 18, no. 1, pp. 1, 2010.
[30] G. Kresse and J. Furthmüller, *Comput. Mater. Sci.*, vol. 6, no. 1, pp. 15, 1996.
[31] G. Kresse and J. Furthmüller, *Phys. Rev. B*, vol. 54, no. 16, pp. 11169, 1996.
[32] P. E. Blöchl, *Phys. Rev. B*, vol. 50, no. 24, pp. 17953, 1994.
[33] G. Kresse and D. Joubert, *Phys. Rev. B*, vol. 59, no. 3, pp. 1758, 1999.
[34] J. P. Perdew, K. Burke, and M. Ernzerhof, *Phys. Rev. Lett.*, vol. 77, no. 18, pp. 3865, 1996.
[35] S. Curiotto, H. Chien, H. Meltzman, P. Wynblatt, G. S. Rohrer, W. D. Kaplan, and D. Chatain, *Acta Mater.*, vol. 59, no. 13, pp. 5320, 2011.
[36] D. Brandon, *Acta Metall.*, vol. 14, no. 11, pp. 1479, 1966.

[37] Y. V. Naidich, N. F. Grigorenko, and V. M. Perevertailo, *J. Cryst. Growth*, vol. 53, no. 2, pp. 261, 1981.